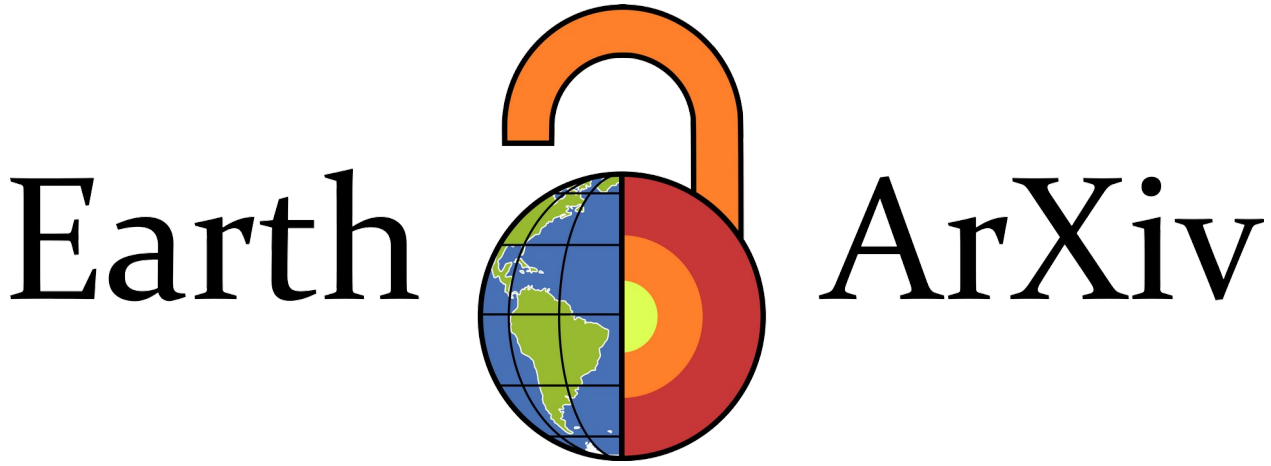

Oxidation state of Mayotte magmatic series: insights from Fe and S K-edge XANES spectroscopy

Charles Le Losq [*α, β], Roberto Moretti[γ], Etienne Médard[δ], Carole Berthod[α, ε], Federica Schiavi[δ], Nicolas Trcera[ζ], and Élodie Lebas[δ]

[α] Université Paris Cité, Institut de physique du globe de Paris, CNRS, F-75005 Paris, France.

[β] Institut Universitaire de France, Paris, France.

[γ] Università degli Studi della Campania "Luigi Vanvitelli", Dipartimento di Ingegneria, I-81031 Aversa (CE), Italy.

[δ] Université Clermont Auvergne, CNRS, IRD, OPGC, Laboratoire Magmas et Volcans, 6 avenue Blaise Pascal, F-63178 Aubière, France.

[ε] Observatoire volcanologique et sismologique de Guadeloupe, Institut de physique du globe de Paris, F-97113 Gourbeyre, France.

[ζ] SOLEIL synchrotron, Saint Aubin, France.

Abstract

Following the 2018-2020 Fani Maoré submarine eruption near Mayotte Island, Indian Ocean, multiple oceanographic expeditions provide unprecedented access to fresh alkaline volcanic glasses spanning basanite to phonolite compositions from the East-Mayotte Volcanic Chain (EMVC). We applied Fe and S K-edge X-ray Absorption Near-Edge Spectroscopy (XANES) to determine iron and sulfur oxidation states in 13 glass samples, providing the first comprehensive redox characterization of this submarine volcanic system. Fe^{3+}/Fe^{TOT} ratios range from 0.19 to 0.51, while S^{6+}/S^{TOT} ratios span 0.02-0.17, with more evolved compositions that tend to show higher oxidation states. Beam damage monitoring revealed significant photo-oxidation effects on sulfur measurements, requiring analysis of initial spectra only. Comparison of redox estimates from multiple independent oxybarometers based on the Fe^{3+}/Fe^{TOT} and S^{6+}/S^{TOT} as well as the olivine-spinel-$a_{SiO_2}^{melt}$ reveals systematic discrepancies between Fe-based and S-based estimates, likely due to Fe-Ti nanolite contamination along X-ray beam paths. Integration of S^{6+}/S^{TOT} measurements with the olivine-spinel-$a_{SiO_2}^{melt}$ oxybarometer indicates ΔFMQ = +0.3 $\pm$ 0.2 for basanite to tephriphonolite magmas, suggesting slightly more oxidized conditions than previously estimated for EMVC. These results provide essential constraints for thermodynamic modeling of alkaline submarine volcanism and highlight the importance of multi-proxy approaches in determining magmatic redox conditions. The oxidation state is consistent with other regional volcanic systems in the SW Indian Ocean, supporting a moderately oxidized mantle source beneath the Comoros archipelago.

Keywords: Mayotte; Xanes; Iron; Sulfur; Redox; Spectroscopy.

1 Introduction

In 2018, a new active submarine volcano, Fani Maoré, was detected via seismic monitoring [Cesca et al. 2020; Lemoine et al. 2020] and observed a year later during the first MAYOBS campaign [Feuillet 2019]. This edifice marks the easternmost part of a 60-km-long WNW-ESE oriented chain (Figure 1), referred to as the EMVC for "East-Mayotte Volcanic Chain" [Bachèlery et al. 2021; Puzenat et al. 2022; Verdurme et al. 2023]. Subsequent campaigns [Rinnert et al. 2019; Thinon and Lebas 2023] allowed for the retrieval of volcanic material from Fani Maoré, as well as from older cones and lava flows, hence providing a comprehensive sampling of extruded magmas along the chain. The EMVC is characterized by the emission of magmas falling

* lelosq@ipgp.fr

along an alkaline basanite-to-phonolite magmatic differentiation trend [Berthod et al. 2021b]. Large effusive flow fields and more explosive dynamism such as the Horseshoe complex are observed [Puzenat et al. 2022]. For Fani Maoré, petrological studies showed that the 2018-2020 eruption was fed by a >35 km deep reservoir, which interacted with an intermediate one before the magma reached the surface [Berthod et al. 2021b]. The basanitic magma was formed by melting of a carbonated mantle source highly enriched in Ba and volatiles [Chauvel et al. 2024]. Pre-eruptive temperature is estimated at 1150 °C at depth, for a basanite magma containing at least 1.2-2.3 wt% water [Berthod et al. 2021a].

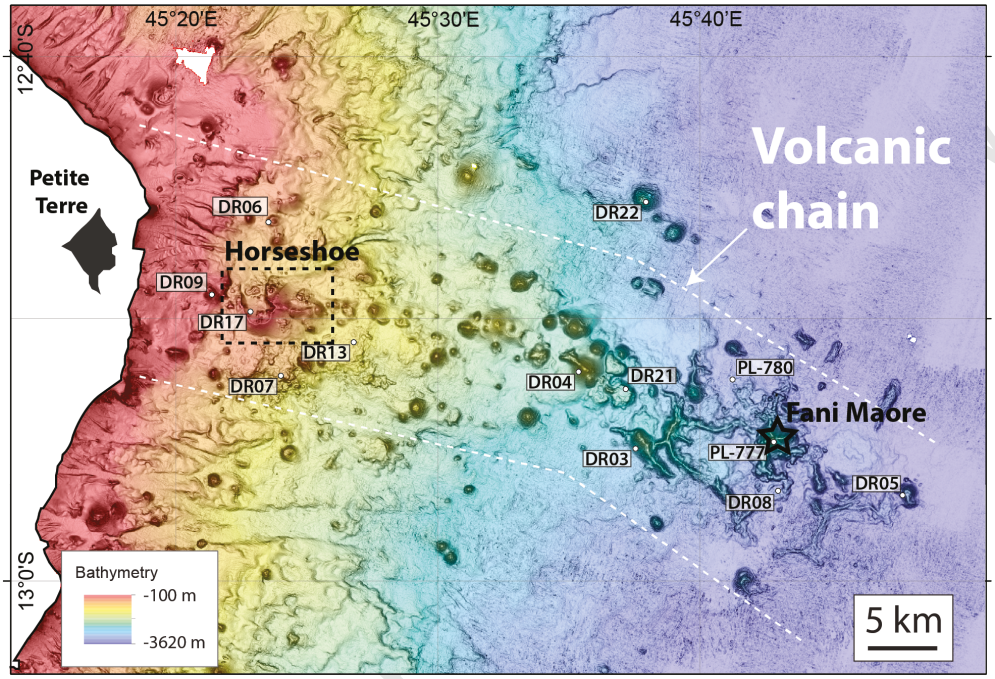

Figure 1: Geological map of the East-Mayotte submarine Volcanic Chain (EMVC) showing the location of the dredges (DR and PL labels) used in this study.

Such estimates of source conditions directly depend on petrological models in which knowledge of the magma oxidation state is key [Carmichael 1991]. Indeed, not only it influences temperature estimates, it also affects the composition of crystallizing phases. It is thus crucial to determine the magma oxidation state to constrain the thermodynamic conditions at the source of the magmatic systems and their subsequent eruptive history [Carmichael 1991; Moussallam et al. 2014; Lierenfeld et al. 2018; Asimow 2021]. Conventionally, the proxy used to infer the magma oxidation state is the Fe^{3+}/Fe^{TOT} ratio measured on volcanic glasses, where $Fe^{TOT} = Fe^{2+}+Fe^{3+}$ [Christie et al. 1986; Berry et al. 2008; Cottrell and Kelley 2011; O'Neill et al. 2018]. Coupling Fe^{3+}/Fe^{TOT} with S^{6+}/S^{TOT}, where $S^{TOT} = S^{6+}+S^{2-}$, may further lead to improved constraints on the oxidation state of magmatic systems [Moretti and Ottonello 2003; Métrich and Mandeville 2010; Moussallam et al. 2014; Brounce et al. 2017; Moretti and Stefánsson 2020; Moretti 2021; Boulliung and Wood 2023]. Such measurements were not yet performed for the Mayotte submarine lavas, a needed knowledge missing for modeling the petrological evolution of EMVC magmas.

We therefore performed X-ray Absorption Near-Edge Spectroscopy (XANES) analysis at the Fe and S K-edges on the LUCIA beamline, SOLEIL synchrotron, on 13 different glass samples representative of the Mayotte magmatic series, including samples from the last-erupted Fani Maoré. XANES spectroscopy is particularly well-suited for this work, as it allows the analysis of the Fe and S redox state on a micrometer scale [Cottrell et al. 2009]. This ability is important as we aim at

getting data from glass, either located at the edge of pillow lava rims for mafic samples (basanites) or between microlites for differentiated ones (phonolites). Beam damage may be a problem during XANES analysis [Lerner et al. 2021]. It was mitigated by using an attenuated beam, and monitored and documented through time series on given spots. The obtained Fe K-edge and S K-edge XANES spectra allow retrieving the Fe^{3+}/Fe^{TOT} and S^{6+}/S^{TOT} ratios of the glass samples. Combined with a model linking sulfur and iron redox [Moretti and Ottonello 2003; Moretti 2005; Moretti and Ottonello 2005], the data bring further constraints on the oxygen and sulfur fugacity at the source of the Mayotte magmas.

2 Experimental Methods

2.1 Samples

The analyzed samples were dredged during four oceanographic campaigns dedicated to volcano monitoring (Figure 1, Table 1) [MAYOBS 1, 2, 4 and 15; Feuillet 2019; Fouquet and Feuillet 2019; Jorry 2019; Rinnert et al. 2020], and one research campaign [GeoFLAMME; Rinnert et al. 2021]. They cover the full basanite-to-phonolite differentiation trend characteristic of the EMVC [Berthod et al. 2021b].

The selected glasses were mounted in epoxy, in a cross-section position allowing rim-to-core observation, and polished using diamond pads. Glasses were analyzed using a Cameca SX Five-tactis electron microprobe at Laboratoire Magmas et Volcans (LMV, Clermont-Ferrand, France). For major elements, we used a 15 kV acceleration and an 8 nA current with a defocused beam (20 µm) to avoid Na-loss during the analysis. Calibration was performed on natural and synthetic oxides: wollastonite (Si, Ca), forsterite (Mg), fayalite (Fe), albite (Na), orthoclase (K, Al), $TiMnO_3$ (Ti, Mn), Cr_2O_3 (Cr) and fluorapatite (P). Minor volatile elements (S, F and Cl) were analyzed during a second session using a 100 nA beam current and 5x20 s counting times. Standards include VG2 glass [S, Dixon et al. 1991], natural scapolite (Cl) and CaF_2 (F). Water concentrations in glasses were analyzed using a Renishaw InVia confocal Raman micro-spectrometer. The analytical procedure follows the external calibration procedure described in [Schiavi et al. 2018], using a set of in-house basanitic standards previously analyzed by FTIR spectrometry [Schiavi et al. 2018].

The chemical compositions of the samples are described in Table 2. Water contents range from 0.7 to 1.3 wt% for the basanites, 1.5 wt% for the tephriphonolite, and from 1.3 to 1.8 wt% for the phonolites (Table 2). S contents range from 50 to 1318 ppm. We note high concentrations in F and Cl, typical of alkaline magmatic series.

Prior to the XANES experiments, we selected crystal-free areas by visual inspection under a binocular microscope and by Raman spectroscopy observations. Raman spectra were recorded using a Horiba HR Evolution spectrometer at IPGP (Paris, France) equipped with an ultra-low frequency Notch filter. The latter allows retrieving Raman signal without any deformation from the laser line at frequencies as low as 10 cm^{-1}. In the Raman spectra, we searched for the absence of sharp peaks in the 600-700 cm^{-1}, indicative of the presence of nanocrystals in glasses [Di Genova et al. 2017]. We further confirmed the absence of crystals and the glassy nature of the selected areas by monitoring the presence of the Boson peak in the Raman spectra [Verdurme et al. 2023]. The selected areas were marked on each sample for XANES analysis. For the basanite compositions, they typically correspond to the outer rims of the pillow lava samples that were quenched rapidly upon contact with seawater [Thivet et al. 2023]. Using Raman spectroscopy, the apparition of nanolites is rapidly visible (within a few 100 µm) when

moving from the rim to the core of the samples. For more evolved phonolitic samples, the crystals are mostly of micrometer size or more, such that they are visible and can be avoided when performing the XANES analysis.

2.2 XANES spectroscopy

After sample selection and pre-characterization, XANES measurements at the S and Fe K-edges were performed in fluorescence mode on the LUCIA beamline at the SOLEIL synchrotron facility, France. The incident beam was focused at 3×3 μm^2 and the photon flux reduced to a value of 10^9 photon/s to limit beam damage. Full Fe K-edge XANES spectra were collected using Si(311) crystals, which allow a resolution of 0.2 eV. We recorded those spectra from 7070.0 to 7250.0 eV, with steps of (i) 2.0 eV between 7070.0 and 7104.0 eV, (ii) 0.05 eV between 7104.0 and 7121.0 eV, (iii) 0.3 eV between 7121.3 and 7160.0 eV, and (iv) 1.0 eV between 7160.0 and 7250.0 eV. To monitor possible effects of beam damage on Fe K-edge XANES, we also acquired several quick scans between 7110.0 and 7117.0 eV (1.0 eV step) consecutively after beam exposure on given spots, and tested attenuating the beam down to 50 % of its nominal flux (see Section 3.1).

Features extracted from Fe K-edge XANES spectra can be related to a glass Fe^{3+}/Fe^{TOT} via various methods [e.g. Berry et al. 2003; Wilke et al. 2004; Magnien et al. 2006; Cottrell et al. 2009]. In particular, the centroid of the pre-edge peak visible between 7110.0 and 7117.0 eV varies depending on the glass Fe^{3+}/Fe^{TOT}, and, given a calibration, it can be used to determine Fe^{3+}/Fe^{TOT} in glass series [Wilke et al. 2004; 2005; Cottrell et al. 2009; Fiege et al. 2017; Zhang et al. 2018]. To calculate the Fe K pre-edge centroid with precision, we first normalize the Fe K-edge XANES spectra using linear functions to fit the pre- and post-edge backgrounds using LARCH [Newville 2013], and then decompose the pre-edge signals using a sum of two pseudo-Voigt peaks and an exponential function, following Le Losq et al. [2020a]. The Fe K pre-edge centroid position is finally calculated from the weighted sum of the areas of the pseudo-Voigt peaks. To calibrate the dependence of the Fe K-pre-edge centroid on glass Fe^{3+}/Fe^{TOT}, we use the PyNa glasses from Magnien et al. [2006] as standards. Those glasses contain ~52.7 wt% SiO_2, ~12.0 wt% MgO, ~5.5 wt% Na_2O, and ~12.8 wt% FeO, and a range of Fe^{3+}/Fe^{TOT} (from 0.09 to 0.95) measured using multiple techniques, including Mössbauer spectroscopy, wet chemistry, microprobe, XANES and Raman spectroscopy [Magnien et al. 2006]. Fe^{3+}/Fe^{TOT} values from the different techniques agree well within the error bar. In the following, we will use as reference values the Mössbauer Fe^{3+}/Fe^{TOT}.

Full S K-edge XANES spectra were collected on the glass samples using a Si(111) crystal. We recorded those spectra between 2455.0 and 2525.0 eV, using (i) a 1.0 eV step between 2455.0 and 2465.0 eV, (ii) a 0.2 eV step between 2465.2 and 2500.0 eV, and (iii) a 1 eV step after the edge between 2500.0 and 2525.0 eV. Using LARCH, we fitted linear backgrounds before and after the edge, which position was taken as half the edge step. To check for possible beam damage, frequent during S K-edge XANES analysis [e.g. Lerner et al. 2021], quick scans of the edge region between 2465.0 and 2485.0 eV were also performed with a step size of 1.0 eV. Those scans took approximately 1 minute to acquire, while the full S K-edge XANES spectra took approximately 5 minutes 30 seconds. Using the SciPy Python library [Virtanen et al. 2020], we implemented the peak fitting method from Lerner et al. [2021] as well as the intensity ratio method of Jugo et al. [2010] to retrieve the redox state of sulfur from the full S K-edge XANES spectra. To be able to also exploit the quick scans that only consist of data every eV, we slightly modified the method of Jugo et al. [2010]: the intensity I6 of the S^{6+} contribution is calculated from the maximum

value retrieved between 2480 and 2485 eV, and the I2 intensity from the S^{2-} contribution is calculated from the median of the signal intensity between 2475 and 2477 eV. Then, using the data from Jugo et al. [2010], we recalibrated the relationship between I6/(I2 + I6) and $S^{6+}/(S^{6+} + S^{2-})$ using a 6-order polynomial function. This ensures that we can use quick scans to retrieve the sulfur redox state (see Results section for details and reasons), and also that any difference in data treatment will not affect $S^{6+}/(S^{6+} + S^{2-})$ estimation.

3 Results

3.1 Fe K-edge spectra

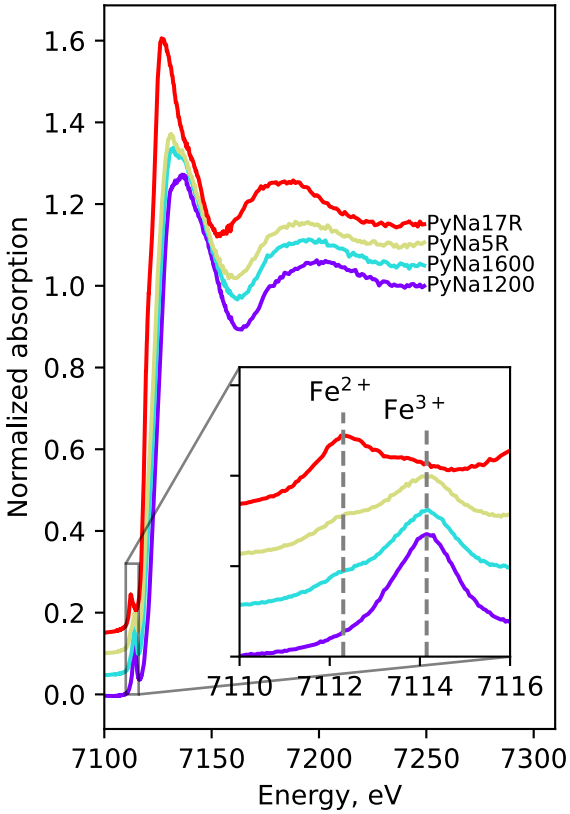

Figure 2: Fe K-edge XANES spectra of the PyNa reference glass materials [Magnien et al. 2006]. The PyNa17R, PyNa5R, PyNa1600 and PyNa1200 have Fe^{3+}/Fe^{TOT} = 0.09 ± 0.02, 0.60 ± 0.02, 0.75 ± 0.02 and 0.95 ± 0.02, respectively. Spectra are shifted vertically for visualization.

The Fe K-edge XANES spectra of the glass standards present an evolution of the pre-edge and edge typical of variations in the Fe oxidation state (Figure 2). Upon oxidation, the Fe K-edge shifts towards a higher energy [Berry et al. 2003]. The shape of the pre-edge, which contains contributions related to the 1s→3d bound state electronic transitions in Fe^{2+} and Fe^{3+} cations [Galoisy et al. 2001; Wilke et al. 2001], also changes (inset in Figure 2). Upon oxidation, we observe decreasing and increasing intensities at ≈7112.3 eV (Fe^{2+} contribution) and ≈7114.1 eV (Fe^{3+} contribution), respectively, in agreement with observations from previous studies [Galoisy et al. 2001; Wilke et al. 2001; Berry et al. 2003; Wilke et al. 2004; Magnien et al. 2006; Cottrell et al. 2009; Zhang et al. 2018; Le Losq et al. 2020b].

The Fe K-pre-edge centroid varies non-linearly with the PyNa glass Fe^{3+}/Fe^{TOT} (Figure 3). Previous authors typically used polynomial equations as calibration lines [e.g. Fiege et al. 2017], but those have the caveat not to be bound between centroid endmember positions for Fe^{2+} and Fe^{3+}. To solve this issue, we used the following equation:

$$C = (1-x) \times C_{Fe^{2+}} + x \times C_{Fe^{3+}} + [x \times (1-x)]^{(w+x)} \quad (1)$$

with C the Fe K pre-edge centroid energy, $x = Fe^{3+}/Fe^{TOT}$, $C_{Fe^{2+}}$ the energy of the maximum of the Fe^{2+} contribution, $C_{Fe^{3+}}$ that of the Fe^{3+} contribution, and w an adjustable parameter. The term $[x \times (1-x)]^{(w+x)}$ enables deviation from a linear trend bound by $C_{Fe^{2+}}$ and $C_{Fe^{3+}}$. A least-square adjustment yielded $w = 0.52$. Using this equation allows obtaining a good fit of the present data (dashed purple line in Figure 3). The root-mean-squared-error (RMSE) between calculated and observed values on PyNa glasses is ±0.009.

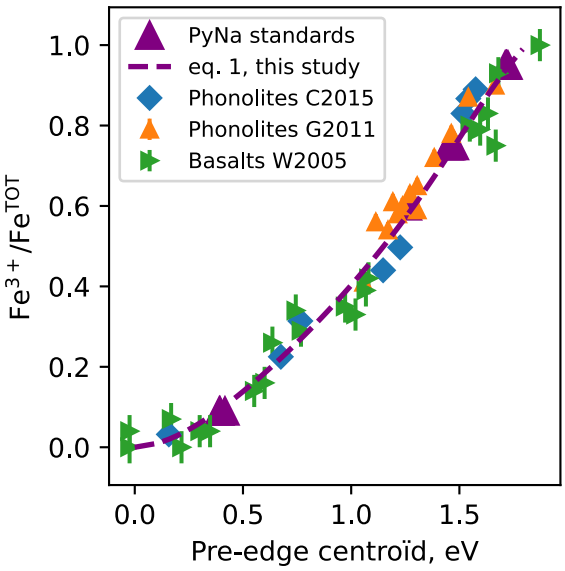

Figure 3: Evolution of the Fe K pre-edge centroid as a function of Fe^{3+}/Fe^{TOT}. Data from previous studies are also reported for comparison [Wilke et al. 2005; Giuli et al. 2011; Berry et al. 2018].

The Fe K pre-edge centroid versus Fe^{3+}/Fe^{TOT} calibration may depend on the composition [Cottrell et al. 2009]. To test if we can use the calibration shown in Figure 3 for alkali-rich Mayotte glass samples, we compared the PyNa Fe K pre-edge centroid versus Fe^{3+}/Fe^{TOT} trend to those reported for other glasses from previous studies. For this comparison, we focus on alkali-rich glasses. Whilst the literature is heavily focused on calc-alkaline compositions [Cottrell et al. 2009; Cottrell and Kelley 2011; Zhang et al. 2017; Berry et al. 2018; Zhang et al. 2018], three studies present Fe K pre-edge XANES centroid positions versus Fe^{3+}/Fe^{TOT} data from Mössbauer spectroscopy and wet chemistry that can allow testing the validity of the present calibration: Wilke et al. [2005] on alkali-rich sodium silicate compositions, and Giuli et al. [2011] and Cicconi et al. [2015] on phonolitic glasses. To plot the data from those studies in the figure Figure 3), we first need to normalize the Fe K pre-edge centroid data, as different data treatments and beamline specifics were applied and may induce shifts between the trends [Fiege et al. 2017]. To normalize the Fe K pre-edge centroids from the literature $C_{reported}$, we used the equation:

$$C_{norm} = \frac{C_{reported} - C_{Fe^{2+}}}{C_{Fe^{3+}} - C_{Fe^{2+}}} \times 1.8 \quad (2)$$

with $C_{Fe^{2+}}$ and $C_{Fe^{3+}}$ the positions of the Fe^{2+} and Fe^{3+} contributions reported by the various studies, and 1.8 the distance between $C_{Fe^{2+}}$ and $C_{Fe^{3+}}$ observed in our study (this acts as a scaling factor). After Fe K pre-edge centroid normalization, we observe that existing data fall well within the general trend of the calibration (purple dashed line, Figure 3). Using the Fe K pre-edge centroids from Wilke et al. [2005], Giuli et al. [2011], and Cicconi et al. [2015] and the present calibration, we reproduce the Fe^{3+}/Fe^{TOT} reported in those studies within ±0.05, in average; the coefficient of determination R^2 between the calibration and data is 0.974. The average error is higher than that affecting the Fe redox state determination in the PyNa glasses, but this is not surprising given the differences in acquisition setups, conditions, and glass compositions between the different studies. Actually, compared to other efforts in implementing general calibrations relating Fe K pre-edge centroid and glass Fe^{3+}/Fe^{TOT}, the present calibration line compares well. For instance, Fiege et al. [2017] report an average error of 6 % and a R^2 of 0.987 for a calibration for glasses with $0.3 \leq Fe^{3+}/Fe^{TOT} \leq 0.85$, implemented on data from only one beamline (13-ID-E at APS, Argonne, U.S.A.).

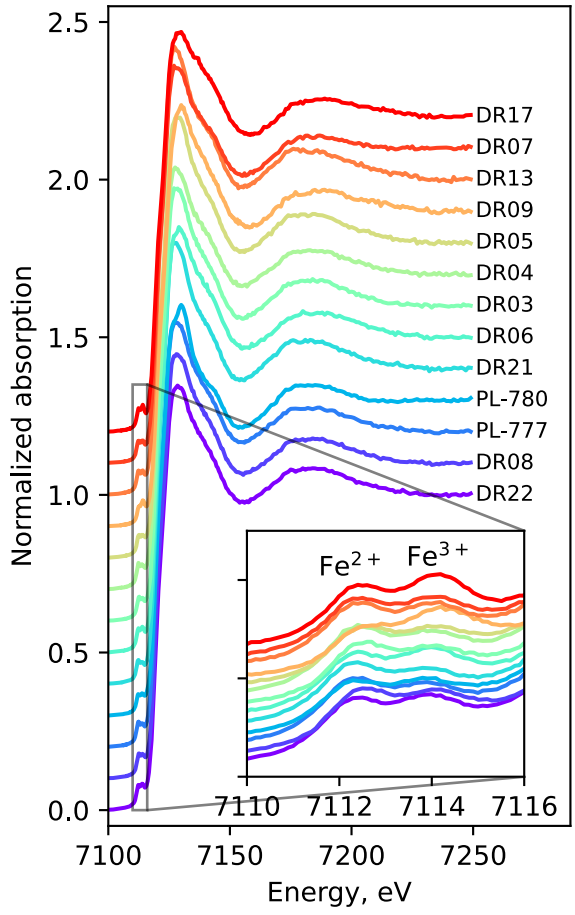

Figure 4: (a) Example of Fe K-edge XANES spectra acquired on the Mayotte dredged samples. In the pre-edge region (see zoom), Fe^{2+} and Fe^{3+} contributions are visible near 7112.3 and 7114.1 eV, respectively. Spectra are shifted vertically for visualization.

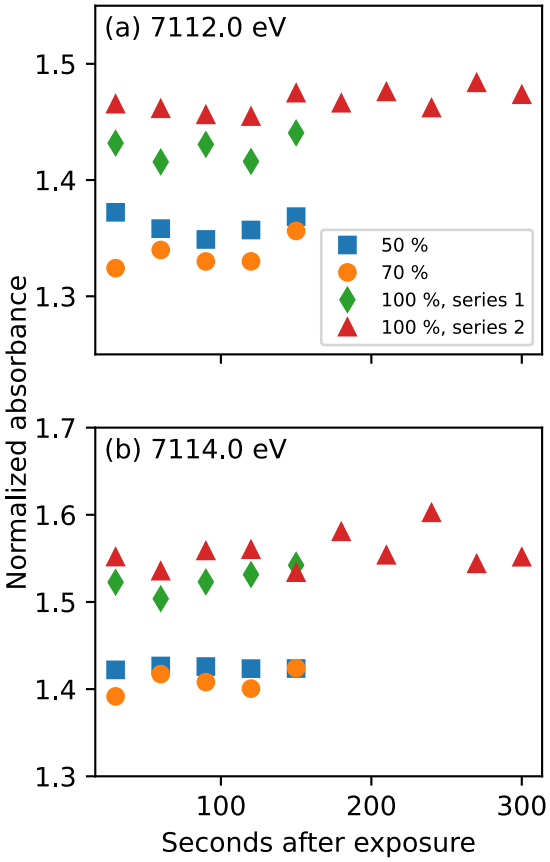

Figure 5: Raw absorbance at 7112.0 (a) and 7114.0 (b) eV and three different beam attenuation conditions. Four time series are displayed for the tephri-basanite sample PL-780.

As we measured Fe^{3+}/Fe^{TOT} on the PyNa and the alkaline magmatic glasses using the same conditions and on the same beamline, this 0.05 value is an upper bound on the uncertainties associated with the measurements presented in this communication. Hence, using Equation 1 with $w = 0.52$ for the present study enables calculation of Fe^{3+}/Fe^{TOT} with a maximum error of 0.05. Small adjustments of w may be necessary for processing data for calc-alkaline magmas, but the general protocol (Equations 1, 2) will remain valid and has the advantages of collapsing several datasets on a unique representation and of circumventing the use of unbound polynomial equations.

With this protocol, Fe K-edge XANES spectra from Mayotte natural glass samples can be processed to obtain Fe^{3+}/Fe^{TOT} given Fe K pre-edge centroids. Figure 4 shows examples of acquired Fe K-edge XANES spectra on the Mayotte samples listed in Table 2. The overall shape of the Fe K-edge XANES spectra indicates that the samples have low to intermediate Fe^{3+}/Fe^{TOT} (Figure 4). This is confirmed by the inspection of the pre-edge region on the Fe K-edge XANES spectra, which reveals significant contributions from both Fe^{2+} and Fe^{3+}. Using the peak fitting procedure to model the pre-edge, we calculated the Fe K pre-edge centroids and then the Fe^{3+}/Fe^{TOT} ratios using the calibration previously presented (Figure 3). The reported results (Table 2) are average values calculated from different spectra. Fe^{3+}/Fe^{TOT} ranges between ≈ 0.19 (DR21) and ≈ 0.51 (DR09). DR21, PL-777, PL-780, DR04 glasses present Fe^{3+}/Fe^{TOT} between 0.20 and 0.24, DR13, DR07, DR06, DR05, DR03,

DR08 between 0.26 and 0.31, and finally DR17 glass Fe^{3+}/Fe^{TOT} = 0.37. The value of ≈ 0.51 for sample DR09 probably is an anomaly: only one Fe K-edge XANES spectrum allowed the calculation of Fe^{3+}/Fe^{TOT}. Without further information, we consider it as an outlier produced, for instance, by a signal affected by that of a neighbor crystal. While it seems that the most evolved samples (phonolites) have the highest Fe^{3+}/Fe^{TOT}, there actually is no obvious correlation between the major element chemical compositions and the Fe^{3+}/Fe^{TOT} of the samples: correlation coefficients between oxide component concentrations and Fe^{3+}/Fe^{TOT} are all below 0.3.

One question surrounds the acquired data: is beam damage a concern? In particular, photo-oxidation can be a problem for H_2O-bearing glasses [Cottrell et al. 2018; Lerner et al. 2021]. To address this question, we turn to the quick scans acquired on four different spots with three different beam attenuation values (50 %, 70 % and 100 % of the incident flux on the sample) on sample PL-780. Those quick scans allow following the time evolution of the absorption at 7112 eV and 7114 eV Figure 5, which roughly correspond to the positions of the Fe^{2+}/Fe^{3+} contributions (Figure 4); any significant change at those energies would reflect changes in Fe^{2+}/Fe^{3+} resulting from beam damage. Between the different time series, differences in raw absorption are observed. They can be explained by slight variations in acquisition conditions, in particular beam flux variations. Indeed, acquisitions performed with an attenuated beam present lower raw absorption than those acquired with no attenuation. Additional instrumental effects probably affect the raw absorbance and explain other differences between the time series. Aside from those, we do not observe systematic variations with time in a given time series. In particular, no systematic absorption decrease at 7112.0 eV and concomitant increase at 7114.0 eV is observed with time. The variations seem to be within acquisition errors. Therefore, if there were beam damage, its effect would be undetectable. This absence of beam damage may be explained by the relatively low water concentration of the present glasses Table 2 and their relatively high fraction of Fe^{3+} [Cottrell et al. 2018].

3.2 S K-edge spectra

Examples of S K-edge XANES spectra acquired on the samples are shown in Figure 6. Unfortunately, within the timeframe of the beamtime allocation, we did not achieve to get spectra for all samples listed in Table 2. Available spectra show variable signal-to-noise ratios due to variations in the total S content the glass samples carry (Table 2). S K-edge XANES spectra of S-poor phonolitic glasses (DR13, DR07 and DR17) present signal-to-noise ratios lower than those of the spectra of S-rich basanites and tephri-basanites. In addition to the overall broad edge, signals near 2476.0 and 2481.7 eV are visible and can be assigned to S^{2-} and S^{6+} contributions, respectively [Jugo et al. 2010; Métrich and Mandeville 2010; Lerner et al. 2021]. The S^{2-} contribution is dominant in samples DR22, DR08, GLF778, PL-780 and DR04. On the contrary, the S^{6+} contribution is intense in the phonolitic glasses DR13, DR07 and DR17. Peaks below 2470 eV are visible in all samples. Another signal near 2466.5 eV is also intense and solely observed in phonolitic samples (DR13, DR07, DR17). Those signals can be assigned to sulfide phases [Métrich et al. 2009]. Finally, we also placed the expected position of the S^{4+} contribution in Figure 6 even though it is not clear if this contribution is visible in the present spectra. It usually occurs because of photo-reduction effects under the beam. In the present case, we do not observe photo-reduction, but photo-oxidation (see below), explaining why it may not contribute intensity to the spectra.

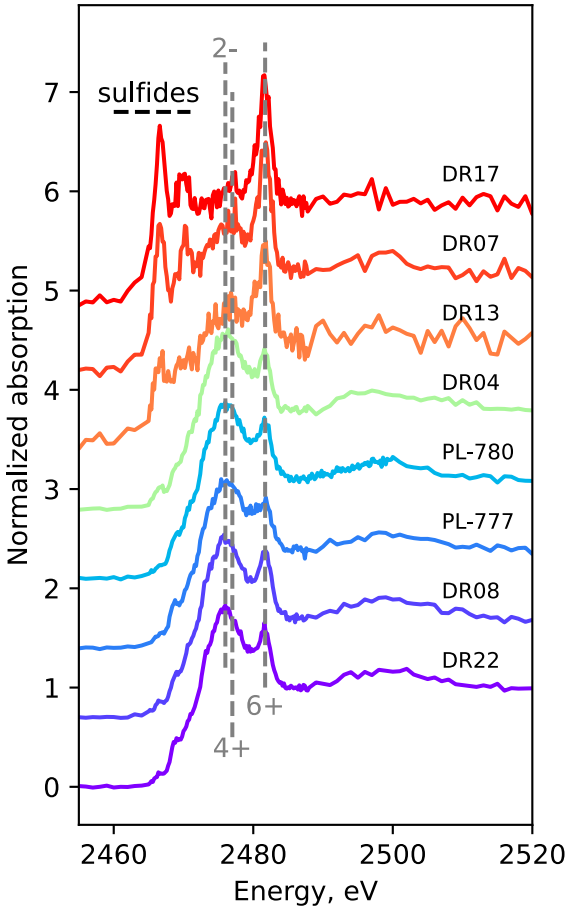

Figure 6: Examples of S K-edge XANES spectra acquired on Mayotte submarine samples. The positions of the contributions from sulfides as well as S^{2-}, S^{4+} and S^{6+} are represented by vertical dashed lines. Spectra are shifted vertically for visualization. See figure 4 for color code.

To extract S^{6+}/S^{TOT} from the S K-edge XANES spectra, we tested the intensity ratio method of Jugo et al. [2010] and the peak fitting method of Lerner et al. [2021]. The intensity ratio method allows calculating the S^{6+}/S^{TOT} via a simple measurement of the ratio of the signal intensities assigned to S^{2-} and S^{6+}. The peak fitting method relies on peak fitting the S K-edge spectra to obtain the areas of two peaks assigned to S^{2-} and S^{6+}, and then relate those to S^{6+}/S^{TOT} via a quadratic equation. Using both methods, we calculated the S^{6+}/S^{TOT} samples for which S K-edge XANES spectra were available. The peak fitting method returned systematically higher S^{6+}/S^{TOT} values compared to the intensity ratio method. Ultimately, we used S^{6+}/S^{TOT} values obtained via the intensity ratio method because this method has shown a good agreement with S^{6+}/S^{TOT} values retrieved from wet chemistry analysis of Mayotte alkaline glasses [Isabelle Genot, IPGP, personal communication].

The detailed review of the S^{6+}/S^{TOT} values revealed an important photo-oxidation effect affecting the data (Figure 7). Depending on the exposure time, S^{6+}/S^{TOT} can increase by 0.01 and up to 0.10. The time series we perform on the DR17 phonolite and DR04 basanite samples reveal a logarithmic trend with time (Figure 7). This makes it difficult to extrapolate back to the original values since the largest changes occur within the first seconds of exposure. We can attempt to retrieve original values by fitting the time series data for DR04 and DR17 with a logarithmic model of the form $y = a + \log(b \times t + 1) + c$, where a, b and c are adjustable parameters and t is the time. This yields estimates of S^{6+}/S^{TOT} at $t = 0$ approximately equal

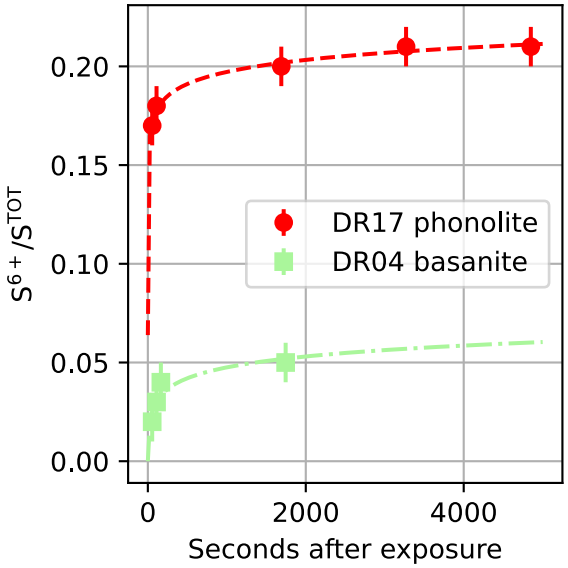

Figure 7: S^{6+}/S^{TOT} as a function of time, for a basanite (DR04) and a phonolite (DR17). Spectra were recorded consecutively at the same position. The increasing S^{6+}/S^{TOT} with time indicate that photo-oxidation under the beam occurred. Dashed and dashed-dotted lines are fits of a logarithmic model of the time-series data (see text).

to 0.00 and 0.06 for DR04 and DR17, respectively. Those values have to be taken with caution because we do not have enough points within the first seconds of exposure to efficiently constrain the fit. However, this analysis suggests that S^{6+}/S^{TOT} may change very significantly during the first seconds of exposition to the photon flux.

To limit the influence of photo-oxidation on the results, we only report S^{6+}/S^{TOT} calculated using the first one or two quick scans at each analysis spot, acquired within the first two minutes of exposure (Table 2). Those values are the least affected by photo-oxidation under the beam. They still are upper bounds as S^{6+}/S^{TOT} may increase rapidly within the first minute (Figure 7). S^{6+}/S^{TOT} values increase with magmatic differentiation. Indeed, basanitic glasses such as PL-780 present S^{6+}/S^{TOT} equal to 0.03 ± 0.01, whereas phonolite glasses such as DR17 present more oxidized S^{6+}/S^{TOT} equal to 0.17 ± 0.01. This trend is confirmed by the statistical analysis : Pearson correlation coefficients R between the molar fractions of major elements and S^{6+}/S^{TOT} range between 0.76 and 0.86, and S^{6+}/S^{TOT} anti-correlates strongly with the magnesium number Mg# ($R = -0.92$).

4 Discussion

4.1 Redox modeling

We can model the Fe and S redox state using a ionic-polymeric model (abbreviated hereafter IPA model) that links melt composition (Table 2), temperature T and pressure P, and oxygen [log $f(O_2)$] and sulfur [log $f(S_2)$] fugacities to the melt's S^{6+}/S^{TOT}, Fe^{3+}/Fe^{TOT} and sulfur concentration at sulfide and sulfate saturation [Moretti 2005; Moretti and Ottonello 2005; Moretti and Ottonello 2022; Moretti 2022].

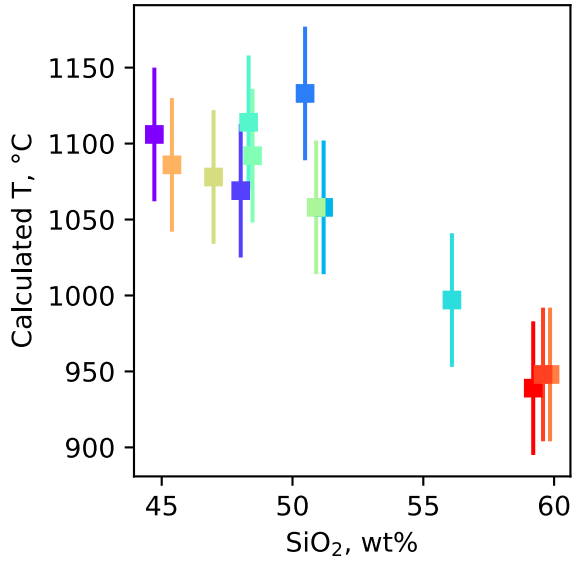

Figure 8: Temperature calculated from the olivine-melt equilibrium represented as a function of the glass silica concentration in wt%. If not visible, error bars are smaller than symbol size. See figure 4 for color code.

First, we estimate temperatures using olivine/melt thermometry [Beattie 1993], correcting for the effect of water [Médard and Grove 2008] (Figure 8). For basanite to phonotephrite compositions, calculated temperatures range between 1050 and 1150 °C. For the tephriphonolite sample DR21, temperature is ≈ 1000 °C. Calculated temperatures for the phonolite samples DR07, DR09 and DR17 are of approximately 950 °C. Such values agree with previous temperature estimates [Berthod et al. 2021a; Lacombe 2023]. Overall, we observe a general decrease of temperature with increasing magmatic differentiation.

With this set of temperatures and the sample chemical compositions (Table 2), we then adjust log $f(O_2)$ values via least-square regression to reproduce the measured Fe^{3+}/Fe^{TOT} or S^{6+}/S^{TOT} values using the IPA model. For those calculations, the pressure was set to 35 MPa, i.e. the average seafloor pressure near the Fani Maoré underwater volcano [Feuillet et al. 2021]. Plausible deviations from this value lead to little change in the results and can be neglected.

When adjusting log $f(O_2)$ values to reproduce the measured Fe^{3+}/Fe^{TOT}, estimated ΔFMQ values range between 0.6 and 3.1, with a median at 1.4 (Figure 9). Values for most samples actually range between 0.6 and 1.6, except for samples DR09 and DR17 that present significantly higher values. At such redox conditions, the IPA model predicts S^{6+}/S^{TOT} equal to or higher than 0.8, well above the measured values.

When adjusting log $f(O_2)$ values to reproduce the measured S^{6+}/S^{TOT}, estimated ΔFMQ values range between -0.6 and -0.1, with a median at -0.4 (Figure 10). The IPA model then returns Fe^{3+}/Fe^{TOT} values of ≈ 0.12 for all samples. We thus observe a discrepancy between log $f(O_2)$ values estimated using either Fe^{3+}/Fe^{TOT} or S^{6+}/S^{TOT}, which result in a significant difference in ΔFMQ.

To check that the observed discrepancy is not model-related, we check log $f(O_2)$ values returned by independent iron and sulfur redox models. Using the measured Fe^{3+}/Fe^{TOT} values and the Borisov et al. [2018] model (abbrev. B2018), we calculate ΔFMQ values ranging between 0.7 and 3.6, with a median of 1.5 (Figure 9). Using the model of Kress and Carmichael [1991] (abbrev. KC1991), ΔFMQ values range between 0.2 and 3.6, with a median of 1.0. The IPA, KC1991 and B2018 models thus

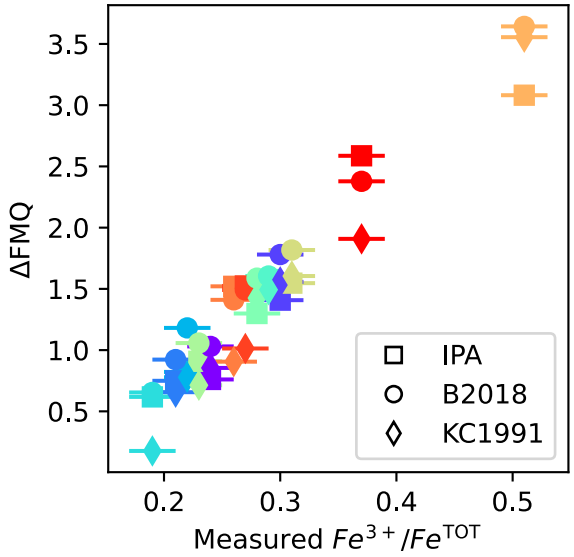

Figure 9: Deviation from the Fayalite-Magnetite-Quartz oxygen buffer (ΔFMQ) calculated using the measured Fe^{3+}/Fe^{TOT} and the IPA model. ΔFMQ values calculated using the KC1991 [Kress and Carmichael 1991] and B2018 [Borisov et al. 2018] models are also represented for comparison. See figure 4 for color code.

return consistent ΔFMQ values, ranging between 0.2 and 3.6 approximately, with medians approximately 1.0-1.5 log units above the FMQ buffer (Figure 9). We finally note that the 3.1-3.5 ΔFMQ value (Figure 9) corresponds to the sample DR09, which has been previously identified as an outlier.

The same comparison can be made using the measured S^{6+}/S^{TOT} values and the models of Boulliung and Wood [2023] (abbrev. BW2023) or Jugo et al. [2010] (abbrev. J2010). Both return similar ΔFMQ values, ranging between 0.0 and 0.8 (Figure 10). Those values are higher than those calculated using the IPA model by ≈ 0.75 log unit, but they still are significantly below the ΔFMQ values calculated from the measured Fe^{3+}/Fe^{TOT}.

Using measured S^{6+}/S^{TOT} values to estimate redox conditions thus yields ΔFMQ values that are systematically lower than those calculated using measured Fe^{3+}/Fe^{TOT} values. The median difference is of ≈ 1.5 log unit when using ΔFMQ values calculated with the IPA model. It decreases to ≈ 0.5 log unit when using ΔFMQ calculated from Kress and Carmichael [1991] and Boulliung and Wood [2023].

4.2 olivine-spinel-$a_{melt}^{SiO_2}$ (OSaS) oxybarometer

We observe a discrepancy between the redox conditions calculated from the sulfur and iron oxidation states measured in glasses. To try deciphering its origin, we further estimated the redox conditions using the olivine-spinel-$a_{melt}^{SiO_2}$ oxybarometer from Bell et al. [2025]. Using electron microprobe, we measured the composition of olivine and spinel phases observed in all glasses but DR17, which does not contain olivine [see for full dataset the Zenodo repository Le Losq et al. 2025]. The oxygen fugacity of the host liquid can then be accessed via a thermodynamic analysis of the olivine-spinel-liquid reaction:

$$3Fe_2SiO_4^{olivine} + O_2^{system} = 2Fe_3O_4^{spinel} + 3SiO_2^{melt} \quad . \tag{3}$$

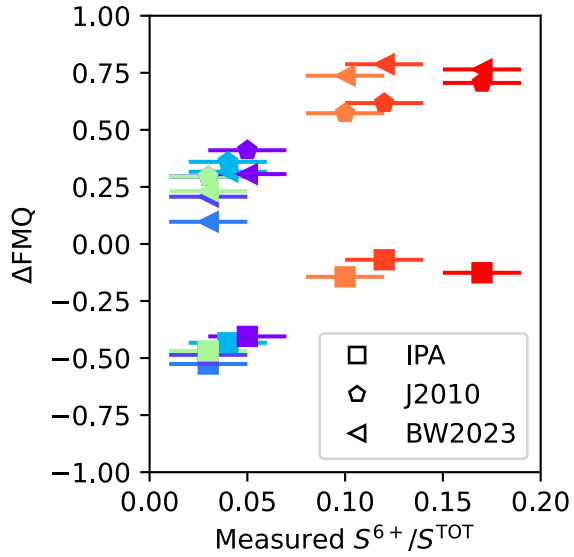

Figure 10: Deviation from the Fayalite-Magnetite-Quartz oxygen buffer (ΔFMQ) calculated using the measured S^{6+}/S^{TOT} and the IPA model. ΔFMQ values calculated using the J2010 [Jugo et al. 2010] or BW2023 [Boulliung and Wood 2023] models are also represented for comparison. See figure 4 for color code.

To perform the calculations, we directly used the MELTS-OSaS software provided by Bell et al. [2025], which uses MELTS to obtain values of the silica activity in the melt, $a_{melt}^{SiO_2}$.

MELTS-OSaS values are reported in Figure 11. We observe that for basanite to phonotephrite compositions, ΔFMQ values are ≈ 0.3. Values for the tephri-phonolite (DR21) and phonolite samples (DR07, DR13, DR17) deviate from this value and become significantly negative.

In Figure 11, we observe that ΔFMQ values estimated from S^{6+}/S^{TOT} using the Boulliung and Wood [2023] model agree well with ΔFMQ values from MELTS-OSaS for basanite to phonotephrite compositions. We propose that this encourages the use of the Boulliung and Wood [2023] model for the present dataset.

Again, ΔFMQ values from Fe^{3+}/Fe^{TOT} measurements systematically diverge from values determined by MELTS-OSaS or S^{6+}/S^{TOT}. In Figure 11, we report ΔFMQ values calculated using measured Fe^{3+}/Fe^{TOT} and the IPA model, corrected for an empirical 0.5 log unit shift. Using this correction allows the alignment of ΔFMQ values from iron and sulfur redox states and MELTS-OSaS calculations for some, but not all, basanite and phonotephrite samples. We further observe that this correction reconciles ΔFMQ values from iron and sulfur oxidation states for two of the phonolite samples, DR07 and DR13.

Overall, given the comparison of ΔFMQ from different oxybarometers, we conclude that ΔFMQ values calculated from the iron oxidation state are probably unreliable. This could be due to the presence of iron nanolites that easily form in such melts [Thivet et al. 2023; Verdurme et al. 2023] or any other re-arrangement of iron coordination and oxidation state upon cooling of the melt, particularly across the glass transition [e.g. Burnham et al. 2015; Le Losq et al. 2020b]. Indeed, while we checked prior to the analysis that the areas we investigated were nanolite-free thanks to Raman spectroscopy, the penetration depth of the Raman laser line is much shallower than that of X-rays, which at 7112 eV is of ≈ 50 µm for basanite glasses and reaches ≈ 80 µm for phonolite glasses. Our samples were not double-polished sections but pieces of pillow rims mounted

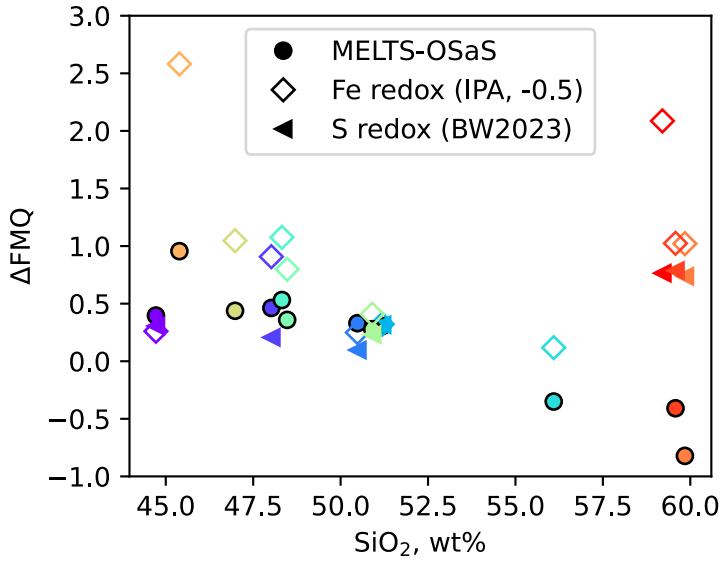

Figure 11: ΔFMQ versus silica concentration (wt%) in the glass samples, using values estimated from S^{6+}/S^{TOT} (BW2023: Boulliung and Wood [2023] method), from Fe^{3+}/Fe^{TOT} (IPA model, shifted by -0.5), and the MELTS-OSaS oxybarometer from Bell et al. [2025]. Error bars are not represented. See figure 4 for color code.

in epoxy. We hypothesize that our analysis could be affected by the presence of some Fe-Ti nanolites along the beam path, with a higher Fe^{3+}/Fe^{TOT} biasing the results. On average, the bias is close to 0.5 log units, but varies from sample to sample (Figure 11). We will thus reject redox values from Fe K-edge XANES spectroscopy in the following.

Considering S^{6+}/S^{TOT} and MELTS-OSaS oxybarometers, we propose that, for basanite to phonotephrite samples, ΔFMQ = 0.3 ± 0.2. For phonolite (DR07, DR13, DR17) and tephriphonolite (DR21) samples, it is more difficult to estimate a reliable redox value. Indeed, S K-edge XANES spectra suggest FMQ + 0.7 while the Bell approach suggests much more reducing conditions, between FMQ - 0.5 and -1.0. The latter values are due to the presence of olivine crystals with low Fo numbers (between Fo_{54} and Fo_{22}), which are impossible to form under oxidizing conditions. We must consider that those samples may have experienced outgassing. Two arguments support this hypothesis. First, they present very low sulfur contents (Table 2) and are sulfide-rich (Figure 6). Secondly, using rhyolite-MELTS 1.2.0 [Ghiorso and Gualda 2015] and simulating the evolution of a basanite (composition DR22) with initially 1 wt% water at ΔFMQ + 0.3, one will find that the phonolites should have more than 2 wt% water, not the 1.6-1.8 wt% actually found in the samples (Table 2). Therefore, it seems plausible that phonolite (DR07, DR13, DR17) and probably the tephriphonolite DR21 samples experienced S and H outgassing in various extents, affecting their sulfur and iron redox states.

4.3 EMVC redox conditions

The EMVC magmas follow a moderately silica-undersaturated alkaline series [Berthod et al. 2021b]. The parental magma originates from the partial melting of a carbonated mantle source highly enriched in Ba [Chauvel et al. 2024]. Fractional crystallization of olivine and pyroxene from this parental magma in a deep mantle-seated magma chamber results in the formation of the basanites [Berthod et al. 2021a]. Modeling using Rhyolite-MELTS suggested that the phonolites are obtained

by further 80% of fractional crystallization of the water-bearing basanite magma at mantle depth under an oxygen fugacity estimated at ΔFMQ - 1 [Berthod et al. 2021b].

The present results suggest redox conditions at ΔFMQ = +0.3 (basanite to tephriphonolite samples), indicating a slightly more oxidized source than initially proposed by [Berthod et al. 2021b]. However, such redox conditions agree with those typical of other regional volcanic systems, such as the Grande Comores or La Réunion which show values near or slightly above FMQ. On La Réunion island, vanadium abundances in olivines indicate redox conditions above FMQ, ranging from 0.2 to 1.5 [Nicklas et al. 2022]. For the Grande Comores, the petrological analysis of peridotite xenoliths from La Grille volcano suggests redox conditions ranging from ≈ FMQ - 0.9 to ≈ FMQ + 0.7 for the underlying mantle [Bordenca et al. 2023]. Redox conditions orbiting slightly above FMQ for the EMVC magmas would thus agree with those previous estimates for the Grande Comores.

5 Conclusion

Using Fe and S K-edge XANES spectroscopy, we measured the iron and sulfur oxidation states in glass samples from the EMVC, including samples from the recent eruption of Fani Maoré. Fe^{3+}/Fe^{TOT} ranges from 0.2 in basanites to 0.37 in phonolites. In parallel, S^{6+}/S^{TOT} ranges from 0.02 to 0.17. The latter values are upper bounds due to S oxidation under the X-ray beam.

Using measured Fe^{3+}/Fe^{TOT} values as well as temperatures calculated from the olivine-melt equilibrium, we estimated redox conditions ranging from ΔFMQ ≈ 0.6 to ≈ 1.6 (leaving aside values from DR17 [crystallized] and DR09 [outlier]). If considering measured S^{6+}/S^{TOT} values, estimated ΔFMQ values are on average 0.5 to 1.5 log units lower, depending on the model. Given this inconsistency, we also assessed the redox conditions using the MELTS-OSaS approach [Bell et al. 2025]. It suggests a ΔFMQ value of 0.3 ± 0.2 for basanite to phonotephrite samples, a value that agrees with estimates from S^{6+}/S^{TOT} values and the Boulliung and Wood [2023] model. Given this, we propose that the source of basanite to phonotephrite magmas at EMVC is at ΔFMQ ≈ 0.3. Further analysis using melt inclusions would be necessary to refine this estimate and, in particular, to better assess the redox conditions of the phonolitic magmas, as the current phonolite samples appear to be affected by outgassing and nanolite formation.

Author Contributions

CLL: sample selection, Raman and XANES experiments, data treatment and interpretation, wrote the manuscript and participated in the final version. RM, NT: XANES experiments, data interpretation, drafted the manuscript and participated in the final version. EM: XANES experiments, sample selection and analysis, data treatment and interpretation, drafted the manuscript and participated in the final version. CB: sample selection and analysis, data treatment and interpretation, drafted the manuscript and participated in the final version. FS: Raman experiments, data interpretation, drafted the manuscript and participated in the final version. EL: data interpretation, drafted the manuscript and participated in the final version.

Acknowledgements

This study has been done as part of proposal 20201492, Lucia beamline, SOLEIL Synchrotron. RM and EM acknowledge the support of the French Agence Nationale de la Recherche (ANR), under grant ANR-22-CE49-0008 (project USB-MAC).

Data Availability

Computer code and data are available on Zenodo [Le Losq et al. 2025], with detailed instructions and a Docker container to easily reproduce the data treatment pipeline used in this study.

References

Christie, D. M., I. S. Carmichael, and C. H. Langmuir (1986). "Oxidation States of Mid-Ocean Ridge Basalt Glasses". *Earth and Planetary Science Letters* 79(3-4), pages 397–411. DOI: 10.1016/0012-821X(86)90195-0.

Carmichael, I. S. E. (1991). "The Redox States of Basic and Silicic Magmas: A Reflection of Their Source Regions?" *Contributions to Mineralogy and Petrology* 106(2), pages 129–141. DOI: 10.1007/BF00306429.

Dixon, J. E., D. A. Clague, and E. M. Stolper (1991). "Degassing History of Water, Sulfur, and Carbon in Submarine Lavas from Kilauea Volcano, Hawaii". *The Journal of Geology*. DOI: 10.1086/629501.

Kress, V. C. and I. S. Carmichael (1991). "The compressibility of silicate liquids containing Fe2O3 and the effect of composition, temperature, oxygen fugacity and pressure on their redox states". *Contributions to Mineralogy and Petrology* 108(1–2), pages 82–92.

Beattie, P. (1993). "Olivine-melt and orthopyroxene-melt equilibria". *Contributions to Mineralogy and Petrology* 115(1), pages 103–111. DOI: 10.1007/BF00712982.

Galoisy, L., G. Calas, and M. Arrio (2001). "High-Resolution XANES Spectra of Iron in Minerals and Glasses: Structural Information from the Pre-Edge Region". *Chemical Geology* 174(1-3), pages 307–319. DOI: 10.1016/S0009-2541(00)00322-3.

Wilke, M., F. Farges, P.-E. Petit, G. E. Brown Jr, and F. Martin (2001). "Oxidation State and Coordination of Fe in Minerals: An Fe K-XANES Spectroscopic Study". *American Mineralogist* 86, pages 714–730.

Berry, A. J., H. S. O'Neill, K. D. Jayasuriya, S. J. Campbell, and G. J. Foran (2003). "XANES Calibrations for the Oxidation State of Iron in a Silicate Glass". *American Mineralogist* 88(7), pages 967–977. DOI: 10.2138/am-2003-0704.

Moretti, R. and G. Ottonello (2003). "Polymerization and Disproportionation of Iron and Sulfur in Silicate Melts: Insights from an Optical Basicity-Based Approach". *Journal of Non-Crystalline Solids* 323(1-3), pages 111–119. DOI: 10.1016/S0022-3093(03)00297-7.

Wilke, M., G. M. Partzsch, R. Bernhardt, and D. Lattard (2004). "Determination of the Iron Oxidation State in Basaltic Glasses Using XANES at the K-edge". *Chemical Geology*. 7th Silicate Melt Workshop 213(1), pages 71–87. DOI: 10.1016/j.chemgeo.2004.08.034.

Moretti, R. (2005). "Polymerisation, Basicity, Oxidation State and Their Role in Ionic Modelling of Silicate Melts". *Annals of Geophysics* 48(4-5). DOI: 10.4401/ag-3221.

Moretti, R. and G. Ottonello (2005). "Solubility and Speciation of Sulfur in Silicate Melts: The Conjugated Toop-Samis-Flood-Grjotheim (CTSFG) Model". *Geochimica et Cosmochimica Acta* 69(4), pages 801–823. DOI: 10.1016/j.gca.2004.09.006.

Wilke, M., G. M. Partzsch, R. Bernhardt, and D. Lattard (2005). "Determination of the Iron Oxidation State in Basaltic Glasses Using XANES at the K-edge". *Chemical Geology* 220(1–2), pages 143–161. DOI: 10.1016/j.chemgeo.2005.03.004.

Magnien, V., D. Neuville, L. Cormier, J. Roux, J.-L. Hazemann, O. Pinet, and P. Richet (2006). "Kinetics of Iron Redox Reactions in Silicate Liquids: A High-Temperature X-ray Absorption and Raman Spectroscopy Study". *Journal of Nuclear Materials* 352(1-3), pages 190–195. DOI: 10.1016/j.jnucmat.2006.02.053.

Berry, A. J., L. V. Danyushevsky, H. S. C. O'Neill, M. Newville, and S. R. Sutton (2008). "Oxidation State of Iron in Komatiitic Melt Inclusions Indicates Hot Archaean Mantle". *Nature* 455(7215), pages 960–963. DOI: 10.1038/nature07377.

Médard, E. and T. L. Grove (2008). "The Effect of H2O on the Olivine Liquidus of Basaltic Melts: Experiments and Thermodynamic Models". *Contributions to Mineralogy and Petrology* 155(4), pages 417–432. DOI: 10.1007/s00410-007-0250-4.

Cottrell, E., K. A. Kelley, A. Lanzirotti, and R. A. Fischer (2009). "High-Precision Determination of Iron Oxidation State in Silicate Glasses Using XANES". *Chemical Geology* 268(3-4), pages 167–179. DOI: 10.1016/j.chemgeo.2009.08.008.

Métrich, N., A. J. Berry, H. S. C. O'Neill, and J. Susini (2009). "The Oxidation State of Sulfur in Synthetic and Natural Glasses Determined by X-ray Absorption Spectroscopy". *Geochimica et Cosmochimica Acta* 73(8), pages 2382–2399. DOI: 10.1016/j.gca.2009.01.025.

Jugo, P. J., M. Wilke, and R. E. Botcharnikov (2010). "Sulfur K-edge XANES Analysis of Natural and Synthetic Basaltic Glasses: Implications for S Speciation and S Content as Function of Oxygen Fugacity". *Geochimica et Cosmochimica Acta* 74(20), pages 5926–5938. DOI: 10.1016/j.gca.2010.07.022.

Métrich, N. and C. W. Mandeville (2010). "Sulfur in Magmas". *Elements* 6(2), pages 81–86. DOI: 10.2113/gselements.6.2.81.

Cottrell, E. and K. A. Kelley (2011). "The Oxidation State of Fe in MORB Glasses and the Oxygen Fugacity of the Upper Mantle". *Earth and Planetary Science Letters* 305(3-4), pages 270–282. DOI: 10.1016/j.epsl.2011.03.014.

Giuli, G., E. Paris, K.-U. Hess, D. B. Dingwell, M. R. Cicconi, S. G. Eeckhout, K. T. Fehr, and P. Valenti (2011). "XAS Determination of the Fe Local Environment and Oxidation State in Phonolite Glasses". *American Mineralogist* 96(4), pages 631–636. DOI: 10.2138/am.2011.3464.

Newville, M. (2013). "Larch: An Analysis Package for XAFS and Related Spectroscopies". *Journal of Physics: Conference Series* 430(1), page 012007. DOI: 10.1088/1742-6596/430/1/012007.

Moussallam, Y., C. Oppenheimer, B. Scaillet, F. Gaillard, P. Kyle, N. Peters, M. Hartley, K. Berlo, and A. Donovan (2014). "Tracking the Changing Oxidation State of Erebus Magmas, from Mantle to Surface, Driven by Magma Ascent and Degassing". *Earth and Planetary Science Letters* 393, pages 200–209. DOI: 10.1016/j.epsl.2014.02.055.

Burnham, A. D., A. J. Berry, H. R. Halse, P. F. Schofield, G. Cibin, and J. F. W. Mosselmans (2015). "The Oxidation State of Europium in Silicate Melts as a Function of Oxygen Fugacity, Composition and Temperature". *Chemical Geology* 411, pages 248–259. DOI: 10.1016/j.chemgeo.2015.07.002.

Cicconi, M. R., G. Giuli, W. Ertel-Ingrisch, E. Paris, and D. B. Dingwell (2015). "The Effect of the [Na/(Na+K)] Ratio on Fe Speciation in Phonolitic Glasses". *American Mineralogist* 100(7), pages 1610–1619. DOI: 10.2138/am-2015-5155.

Ghiorso, M. S. and G. A. R. Gualda (2015). "An H2O–CO2 mixed fluid saturation model compatible with rhyolite-MELTS". *Contributions to Mineralogy and Petrology* 169(6), page 53. DOI: 10.1007/s00410-015-1141-8.

Brounce, M., E. Stolper, and J. Eiler (2017). "Redox Variations in Mauna Kea Lavas, the Oxygen Fugacity of the Hawaiian Plume, and the Role of Volcanic Gases in Earth's Oxygenation". *Proceedings of the National Academy of Sciences* 114(34), pages 8997–9002. DOI: 10.1073/pnas.1619527114.

Di Genova, D., S. Sicola, C. Romano, A. Vona, S. Fanara, and L. Spina (2017). "Effect of Iron and Nanolites on Raman Spectra of Volcanic Glasses: A Reassessment of Existing Strategies to Estimate the Water Content". *Chemical Geology* 475(Supplement C), pages 76–86. DOI: 10.1016/j.chemgeo.2017.10.035.

Fiege, A., P. Ruprecht, A. C. Simon, A. S. Bell, J. Göttlicher, M. Newville, T. Lanzirotti, and G. Moore (2017). "Calibration of Fe XANES for High-Precision Determination of Fe Oxidation State in Glasses: Comparison of New and Existing Results Obtained at Different Synchrotron Radiation Sources". *American Mineralogist* 102(2), pages 369–380. DOI: 10.2138/am-2017-5822.

Zhang, H. L., M. M. Hirschmann, E. Cottrell, and A. C. Withers (2017). "Effect of Pressure on $Fe^{3+}/\Sigma Fe$ Ratio in a Mafic Magma and Consequences for Magma Ocean Redox Gradients". *Geochimica et Cosmochimica Acta* 204, pages 83–103. DOI: 10.1016/j.gca.2017.01.023.

Berry, A. J., G. A. Stewart, H. S. C. O'Neill, G. Mallmann, and J. F. W. Mosselmans (2018). "A Re-Assessment of the Oxidation State of Iron in MORB Glasses". *Earth and Planetary Science Letters* 483, pages 114–123. DOI: 10.1016/j.epsl.2017.11.032.

Borisov, A., H. Behrens, and F. Holtz (2018). "Ferric/ferrous ratio in silicate melts: a new model for 1 atm data with special emphasis on the effects of melt composition". *Contributions to Mineralogy and Petrology* 173(12), page 98. DOI: 10.1007/s00410-018-1524-8.

Cottrell, E., A. Lanzirotti, B. O. Mysen, S. Birner, K. A. Kelley, R. E. Botcharnikov, F. A. Davis, and M. Newville (2018). "A Mössbauer-based XANES Calibration for Hydrous Basalt Glasses Reveals Radiation-Induced Oxidation of Fe". *American Mineralogist* 103(4), pages 489–501. DOI: 10.2138/am-2018-6268.

Lierenfeld, M. B., Z. Zajacz, O. Bachmann, and P. Ulmer (2018). "Sulfur Diffusion in Dacitic Melt at Various Oxidation States: Implications for Volcanic Degassing". *Geochimica et Cosmochimica Acta* 226, pages 50–68. DOI: 10.1016/j.gca.2018.01.026.

O'Neill, H. S. C., A. J. Berry, and G. Mallmann (2018). "The Oxidation State of Iron in Mid-Ocean Ridge Basaltic (MORB) Glasses: Implications for Their Petrogenesis and Oxygen Fugacities." *Earth and Planetary Science Letters* 504, pages 152–162. DOI: 10.1016/j.epsl.2018.10.002.

Schiavi, F., N. Bolfan-Casanova, A. C. Withers, E. Médard, M. Laumonier, D. Laporte, T. Flaherty, and A. Gómez-Ulla (2018). "Water Quantification in Silicate Glasses by Raman Spectroscopy: Correcting for the Effects of Confocality, Density and Ferric Iron". *Chemical Geology* 483, pages 312–331. DOI: 10.1016/j.chemgeo.2018.02.036.

Zhang, H. L., E. Cottrell, P. A. Solheid, K. A. Kelley, and M. M. Hirschmann (2018). "Determination of $Fe^{3+}/\Sigma Fe$ of XANES Basaltic Glass Standards by Mössbauer Spectroscopy and Its Application to the Oxidation State of Iron in MORB". *Chemical Geology* 479, pages 166–175. DOI: 10.1016/j.chemgeo.2018.01.006.

Feuillet, N. (2019). "MAYOBS1 Cruise, RV Marion Dufresne". *French Oceanographic Cruises*. DOI: 10.17600/18001217.

Fouquet, Y. and N. Feuillet (2019). "MAYOBS4 Cruise, RV Marion Dufresne". *French Oceanographic Cruises*. DOI: 10.17600/18001238.

Jorry, S. (2019). "MAYOBS2 Cruise, RV Marion Dufresne". *French Oceanographic Cruises*. DOI: 10.17600/18001222.

Rinnert, E., E. Lebas, J.-C. Komorowski, F. Paquet, S. Jorry, N. Feuillet, I. Thinon, and Y. Fouquet (2019). "MAYOBS". *French Oceanographic Cruises*. DOI: 10.18142/291.

Cesca, S., J. Letort, H. N. T. Razafindrakoto, S. Heimann, E. Rivalta, M. P. Isken, M. Nikkhoo, L. Passarelli, G. M. Petersen, F. Cotton, and T. Dahm (2020). "Drainage of a Deep Magma Reservoir near Mayotte Inferred from Seismicity and Deformation". *Nature Geoscience* 13(1), pages 87–93. DOI: 10.1038/s41561-019-0505-5.

Le Losq, C., M. R. Cicconi, and D. Neuville (2020a). "Iron in Silicate Glasses and Melts: Implications for Volcanological Processes". *Earth and Space Science Open Archive*. DOI: 10.1002/essoar.10503261.1.

Le Losq, C., R. Moretti, C. Oppenheimer, F. Baudelet, and D. R. Neuville (2020b). "In Situ XANES Study of the Influence of Varying Temperature and Oxygen Fugacity on Iron Oxidation State and Coordination in a Phonolitic Melt". *Contributions to Mineralogy and Petrology* 175(7), page 64. DOI: 10.1007/s00410-020-01701-4.

Lemoine, A., P. Briole, D. Bertil, A. Roullé, M. Foumelis, I. Thinon, D. Raucoules, M. de Michele, P. Valty, and R. Hoste Colomer (2020). "The 2018–2019 Seismo-Volcanic Crisis East of Mayotte, Comoros Islands: Seismicity and Ground Deformation Markers of an Exceptional Submarine Eruption". *Geophysical Journal International* 223(1), pages 22–44. DOI: 10.1093/gji/ggaa273.

Moretti, R. and A. Stefánsson (2020). "Volcanic and Geothermal Redox Engines". *Elements* 16(3), pages 179–184. DOI: 10.2138/gselements.16.3.179.

Rinnert, E., I. Thinon, and N. Feuillet (2020). "MD 228 / MAYOBS15 Cruise, RV Marion Dufresne". *French Oceanographic Cruises*. DOI: 10.17600/18001745.

Virtanen, P., R. Gommers, T. E. Oliphant, M. Haberland, T. Reddy, D. Cournapeau, E. Burovski, P. Peterson, W. Weckesser, J. Bright, S. J. van der Walt, M. Brett, J. Wilson, K. J. Millman, N. Mayorov, A. R. J. Nelson, E. Jones, R. Kern, E. Larson, C. J. Carey, İ. Polat, Y. Feng, E. W. Moore, J. VanderPlas, D. Laxalde, J. Perktold, R. Cimrman, I. Henriksen, E. A. Quintero, C. R. Harris, A. M. Archibald, A. H. Ribeiro, F. Pedregosa, and P. van Mulbregt (2020). "SciPy 1.0: Fundamental Algorithms for Scientific Computing in Python". *Nature Methods* 17(3), pages 261–272. DOI: 10.1038/s41592-019-0686-2.

Asimow, P. D. (2021). "The Petrological Consequences of the Estimated Oxidation State of Primitive MORB Glass". In: *Magma Redox Geochemistry*. American Geophysical Union (AGU). Chapter 7, pages 139–154. ISBN: 978-1-119-47320-6. DOI: 10.1002/9781119473206.ch7.

Bachèlery, P., L. Gurioli, J.-C. Komorowski, A. Peltier, J. M. Saurel, A. Lemarchand, and REVOSIMA consortium (2021). *European Catalogue of Volcanoes*. https://volcanoes.eurovolc.eu/?volcano=MAY#.

Berthod, C., E. Médard, P. Bachèlery, L. Gurioli, A. Di Muro, A. Peltier, J.-C. Komorowski, M. Benbakkar, J.-L. Devidal, J. Langlade, P. Besson, G. Boudon, E. Rose-Koga, C. Deplus, A. Le Friant, M. Bickert, S. Nowak, I. Thinon, P. Burckel, S. Hidalgo, M. Kaliwoda, S. J. Jorry, Y. Fouquet, and N. Feuillet (2021a). "The 2018-Ongoing Mayotte Submarine Eruption:

Magma Migration Imaged by Petrological Monitoring". *Earth and Planetary Science Letters* 571, page 117085. DOI: 10.1016/j.epsl.2021.117085.

Berthod, C., E. Médard, A. Di Muro, T. Hassen Ali, L. Gurioli, C. Chauvel, J.-C. Komorowski, P. Bachèlery, A. Peltier, M. Benbakkar, J.-L. Devidal, P. Besson, A. Le Friant, C. Deplus, S. Nowak, I. Thinon, P. Burckel, S. Hidalgo, N. Feuillet, S. Jorry, and Y. Fouquet (2021b). "Mantle Xenolith-Bearing Phonolites and Basanites Feed the Active Volcanic Ridge of Mayotte (Comoros Archipelago, SW Indian Ocean)". *Contributions to Mineralogy and Petrology* 176(10), page 75. DOI: 10.1007/s00410-021-01833-1.

Feuillet, N., S. Jorry, W. C. Crawford, C. Deplus, I. Thinon, E. Jacques, J. M. Saurel, A. Lemoine, F. Paquet, C. Satriano, C. Aiken, O. Foix, P. Kowalski, A. Laurent, E. Rinnert, C. Cathalot, J.-P. Donval, V. Guyader, A. Gaillot, C. Scalabrin, M. Moreira, A. Peltier, F. Beauducel, R. Grandin, V. Ballu, R. Daniel, P. Pelleau, J. Gomez, S. Besançon, L. Geli, P. Bernard, P. Bachelery, Y. Fouquet, D. Bertil, A. Lemarchand, and J. Van der Woerd (2021). "Birth of a Large Volcanic Edifice Offshore Mayotte via Lithosphere-Scale Dyke Intrusion". *Nature Geoscience* 14(10), pages 787–795. DOI: 10.1038/s41561-021-00809-x.

Lerner, A. H., M. J. Muth, P. J. Wallace, A. Lanzirotti, M. Newville, G. A. Gaetani, P. Chowdhury, and R. Dasgupta (2021). "Improving the Reliability of Fe- and S-XANES Measurements in Silicate Glasses: Correcting Beam Damage and Identifying Fe-oxide Nanolites in Hydrous and Anhydrous Melt Inclusions". *Chemical Geology* 586, page 120610. DOI: 10.1016/j.chemgeo.2021.120610.

Moretti, R. (2021). "Ionic Syntax and Equilibrium Approach to Redox Exchanges in Melts". In: *Magma Redox Geochemistry*. American Geophysical Union (AGU). Chapter 6, pages 115–138. ISBN: 978-1-119-47320-6. DOI: 10.1002/9781119473206.ch6.

Rinnert, E., C. Cathalot, and N. Feuillet (2021). "GEOFLAMME Cruise, RV Pourquoi Pas ?" *French Oceanographic Cruises*. DOI: 10.17600/18001297.

Moretti, R. and G. Ottonello (2022). "Silicate Melt Thermochemistry and the Redox State of Magmas". In: *Geological Melts*. Volume 87. Reviews in Mineralogy & Geochemistry. Mineralogical Society of America, pages 339–403.

Moretti, R. (2022). "Redox behavior of degassing magmas: critical review and comparison of glass-based oxybarometers with application to Etna volcano". *Comptes Rendus. Géoscience* 354(S1), pages 249–279. DOI: 10.5802/crgeos.135.

Nicklas, R., R. Hahn, and J. Day (2022). "Oxidation of La Réunion Lavas with MORB-like fO2 by Assimilation". *Geochemical Perspectives Letters* 20, pages 32–36. DOI: 10.7185/geochemlet.2205.

Puzenat, V., N. Feuillet, J.-C. Komorowski, J. Escartín, C. Deplus, P. Bachèlery, C. Berthod, L. Gurioli, C. Scalabrin, C. Cathalot, E. Rinnert, B. Loubrieu, D. Pierre, M. Pitel-Roudaut, N. Tanguy, Y. Fouquet, S. J. Jorry, E. Lebas, F. Paquet, and I. Thinon (2022). "Volcano-Tectonic Structures of Mayotte's Upper Submarine Slope: Insights from High-Resolution Bathymetry and in-Situ Imagery from a Deep-Towed Camera". *Comptes Rendus. Géoscience* 354(S2), pages 81–104. DOI: 10.5802/crgeos.175.

Bordenca, C. V., B. Faccini, A. Caracausi, M. Coltorti, A. Di Muro, T. Ntaflos, R. Pik, A. L. Rizzo, M. Liuzzo, and A. Aiuppa (2023). "Geochemical Evidence for a Lithospheric Origin of the Comoros Archipelago (Indian Ocean) as Revealed by Ultramafic Mantle Xenoliths from La Grille Volcano". *Lithos* 462–463, page 107406. DOI: 10.1016/j.lithos.2023.107406.

Boulliung, J. and B. J. Wood (2023). "Sulfur Oxidation State and Solubility in Silicate Melts". *Contributions to Mineralogy and Petrology* 178(8), page 56. DOI: 10.1007/s00410-023-02033-9.

Lacombe, T. (2023). "Basaltic and phonolitic volcanism of Petite Terre (Mayotte, Indian Ocean): contribution to the comprehension of the on-going sismo-volcanic crisis and associated hazards". PhD thesis. Université Clermont Auvergne.

Thinon, I. and E. Lebas (2023). "MD242 / MAYOBS25 Cruise, RV Marion Dufresne". *French Oceanographic Cruises*. DOI: 10.17600/18003404.

Thivet, S., L. Pereira, N. Menguy, É. Médard, P. Verdurme, C. Berthod, D. Troadec, K.-U. Hess, D. B. Dingwell, and J.-C. Komorowski (2023). "Metastable Liquid Immiscibility in the 2018–2021 Fani Maoré Lavas as a Mechanism for Volcanic Nanolite Formation". *Communications Earth & Environment* 4(1), pages 1–14. DOI: 10.1038/s43247-023-01158-w.

Verdurme, P., C. Le Losq, O. Chevrel, S. Pannefieu, E. Médard, C. Berthod, J.-C. Komorowski, P. Bachèlery, D. R. Neuville, and L. Gurioli (2023). "Viscosity of Crystal-Free Silicate Melts from the Active Submarine Volcanic Chain of Mayotte". *Chemical Geology* 620, page 121326. DOI: 10.1016/j.chemgeo.2023.121326.

Chauvel, C., E. C. Inglis, P. Gutierrez, T.-H. Luu, P. Burckel, and P. Besson (2024). "Fani Maoré, a New "Young HIMU" Volcano with Extreme Geochemistry". *Earth and Planetary Science Letters* 626, page 118529. DOI: 10.1016/j.epsl.2023.118529.

Bell, A. S., L. E. Waters, and M. Ghiorso (2025). "The olivine-spinel-$a^{melt}_{SiO_2}$ (OSaS) oxybarometer: A new method for evaluating magmatic oxygen fugacity in olivine-phyric basalts". *American Mineralogist* 110(1). Edited by C. E. Lesher, pages 48–64. DOI: 10.2138/am-2023-9021.

Le Losq, C., R. Moretti, É. Médard, C. Berthod, F. Schiavi, N. Trcera, and É. Lebas (2025). *charlesll/xanes-mayotte: 1.0.2 (1.0.2)*. Version 1.0.2. DOI: 10.5281/zenodo.17713803.

Table 1: Sample names, references and localization information. abbrev.: short name used in the text and figures.

Dredges	Oceanographic Campaigns	DOI	Samples Name	abbrev.	Start dredging			End dredging		
					Latitude	Longitude	Depth (m)	Latitude	Longitude	Depth (m)
DR03	MAYOBS 1	10.17600/18001217	MAY01-DR03-02-01	DR03	-12.9138	45.6250	2840	-12.9117	45.6280	2590
DR04	MAYOBS 1	10.17600/18001217	MAY01-DR04-06	DR04	-12.8680	45.5887	2315	-12.8662	45.5908	2100
DR05	MAYOBS 1	10.17600/18001217	MAY01-DR05-04-01	DR05	-12.9467	45.7958	3340	-12.9432	45.7985	3190
DR06	MAYOBS 2	10.17600/18001222	MAY02-DR06-02-01	DR06	-12.7712	45.3977	1267	-12.7712	45.3913	1429
DR07	MAYOBS 2	10.17600/18001222	MAY02-DR07-02-07	DR07	-12.8725	45.4077	1590	-12.8680	45.3993	1585
DR08	MAYOBS 2	10.17600/18001222	MAY02-DR08-02	DR08	-12.9450	45.7090	3072	-12.9410	45.7150	3050
DR09	MAYOBS 4	10.17600/18001238	MAY04-DR09-01-05	DR09	-12.8140	45.3570	1125	-12.8165	45.3558	945
DR013	MAYOBS 15	10.17600/18001745	MAY15-DR13-01-01	DR13	-12.8565	45.4532	2220	-12.8462	45.4453	1890
DR017	MAYOBS 15	10.17600/18001745	MAY15-DR17-04-02	DR17	-12.8312	45.3823	1370	-12.8312	45.3790	1340
DR021	GeoFLAMME	10.17600/18001297	GFL-DR21-01-01	DR21	-12.8740	45.6202	2719	-12.8768	45.6187	2629
DR022	GeoFLAMME	10.17600/18001297	GFL-DR22-02-03	DR22	-12.7502	45.6328	3139	-12.7575	45.6310	2756

ROV Dive					Sample location		
					Latitude	Longitude	Depth
PL_777_08	GeoFLAMME	10.17600/18001297	GFL-PL777-08-PBT01	PL-777	-12.911	45.712	2259
PL_780_11	GeoFLAMME	10.17600/18001297	GFL-PL-780-11-07	PL-780	-12.871	45.685	3254

Table 2: Sample names and chemical compositions, in weight percent for major elements and in ppm for S, F and Cl. FeO^*: total concentration in iron provided as FeO. The second row for each sample is the 1σ error bar on measurements. n.a.: not analysed.

sample	SiO_2	TiO_2	Al_2O_3	FeO^*	MnO	MgO	CaO	Na_2O	K_2O	P_2O_5	H_2O	S	F	Cl	Fe^{3+}/Fe^{TOT}	S^{6+}/S^{TOT}
DR22	44.72	3.86	14.09	12.88	0.23	4.71	10.17	4.68	2.71	1.93	1.03	1218	1898	1573	0.24	0.05
	0.18	0.10	0.12	0.24	0.05	0.06	0.13	0.11	0.07	0.15	0.06	107	400	108	0.01	0.01
DR09	45.39	3.41	15.92	11.93	0.21	4.53	11.36	3.94	2.36	0.96	0.88	918	1437	1294	0.51	n.a.
	0.32	0.07	0.17	0.20	0.05	0.06	0.07	0.28	0.06	0.10	0.02	94	375	102	0.01	n.a.
DR05	46.98	3.85	14.41	11.77	0.22	4.06	9.23	4.94	3.07	1.44	n.a.	1318	1872	1417	0.31	n.a.
	0.35	0.10	0.14	0.18	0.04	0.08	0.21	0.16	0.05	0.19		111	398	105	0.01	n.a.
DR08	48.02	2.89	15.59	11.51	0.24	3.76	8.55	5.16	2.99	1.26	1.26	1061	1726	1289	0.30	0.03
	0.13	0.13	0.08	0.18	0.04	0.03	0.12	0.05	0.06	0.08	0.04	100	392	102	0.01	0.01
DR06	48.32	2.62	15.17	11.95	0.29	3.90	7.45	5.32	3.40	1.57	0.73	643	1478	1774	0.29	n.a.
	0.18	0.14	0.10	0.14	0.04	0.09	0.08	0.19	0.07	0.10	0.02	81	378	113	0.01	n.a.
DR03	48.47	2.57	15.21	12.13	0.27	3.86	7.44	5.22	3.15	1.66	1.14	1072	2357	1147	0.28	n.a.
	0.73	0.08	0.23	0.11	0.05	0.12	0.19	0.15	0.99	0.09	0.05	101	423	98		
DR04	50.90	2.37	15.93	10.14	0.25	3.05	6.81	5.92	3.39	1.20	1.25	815	1392	1412	0.23	0.03
	0.25	0.11	0.11	0.18	0.05	0.08	0.11	0.08	0.05	0.09	0.06	89	374	105	0.01	0.02
PL-777	50.48	2.72	16.42	10.43	0.22	3.33	6.87	5.04	2.94	1.49	0.96	869	1830	957	0.21	0.03
	0.21	0.12	0.14	0.17	0.05	0.03	0.09	0.08	0.07	0.06	0.05	92	393	93	0.01	0.01
PL-780	51.19	2.72	16.82	9.85	0.23	3.22	6.78	4.96	2.87	1.23	1.15	985	1568	718	0.22	0.04
	0.35	0.14	0.16	0.13	0.04	0.02	0.07	0.07	0.06	0.14	0.04	97	385	86	0.01	0.01
DR21	56.09	1.15	17.81	7.91	0.20	1.45	3.88	6.76	4.26	0.47	1.53	393	1231	1240	0.24	n.a.
	0.25	0.06	0.16	0.21	0.03	0.01	0.07	0.22	0.07	0.07	0.10	70	359	100	0.01	n.a.
DR13	59.85	0.24	18.59	5.56	0.25	0.29	1.36	7.62	6.02	0.21	1.61	115	1679	1492	0.26	0.10
	0.23	0.02	0.14	0.12	0.03	0.03	0.13	0.10	0.08	0.11	0.10	34	234	67	0.01	0.02
DR07	59.58	0.21	18.70	5.68	0.24	0.32	1.26	7.70	6.13	0.16	1.78	111	1678	1557	0.27	0.12
	0.15	0.03	0.09	0.05	0.04	0.04	0.04	0.11	0.08	0.03	0.09	35	236	69	0.01	0.01
DR17	59.20	0.05	19.49	5.05	0.23	0.06	1.09	8.86	5.90	0.06	1.27	50	2234	2301	0.37	0.17
	0.20	0.02	0.14	0.19	0.05	0.02	0.03	0.09	0.06	0.04	0.05	31	248	80	0.01	0.01